ENG. Struct. Civ. Eng. 2026, 20(3): 623–644
https://doi.org/10.1007/s11709-026-1281-0

RESEARCH ARTICLE

Experimental and numerical study of π-shaped hybrid bridge piers with steel cap beam and innovative joint designs

Chong SHEN[a,b,c], Qingtian SU[a,d], Sizhe WANG[a,e*], Chong WU[a], Jinguo LI[f]

[a] *Department of Bridge Engineering, Tongji University, Shanghai 200092, China*
[b] *Department of Urban Management, Kyoto University, Kyoto 606-8501, Japan*
[c] *Administrative Service Center of Shanghai Municipal Commission of Housing, Urban-Rural Development and Management, Shanghai 200092, China*
[d] *Shanghai Engineering Research Center of High Performance Composite Bridges, Shanghai 200092, China*
[e] *Singapore Centre for 3D Printing, Nanyang Technological University, Singapore 639798, Singapore*
[f] *Tongji Architectural Design (Group) Co., Ltd., Shanghai 200092, China*
[*] *Corresponding author. E-mail: sizhe.wang@ntu.edu.sg*

ABSTRACT To address the transportation and hoisting difficulties caused by excessive self-weights of traditional concrete cap beams, π-shaped hybrid piers with prefabricated steel cap beams and concrete columns were proposed. Moreover, two innovative cap beam–column joint designs using the flange-rebar-ultra high performance concrete (UHPC) connection and the rebar-concrete connection, were developed. Two large-scale (1:4) specimens of hybrid piers with different joint configurations were tested. Both specimens failed due to local buckling at the web and bottom plates of steel cap beams, while the joints and concrete columns remained integrity. They exhibited ultimate bearing capacities of 1023 and 878 kN, with maximum vertical displacements of 59.8 and 21.5 mm at the cantilever beam ends, respectively. Finite element (FE) models well simulated the behavior of hybrid piers and indicated that structural details of steel cap beams, such as stiffeners and discontinuity conditions, affected the ultimate bearing capacity. FE analysis further assessed the influence of construction sequences. Combining an innovative construction method of hinged to rigid with the flange-rebar-UHPC joint, optimized the tensile stress of concrete columns by 49%, mitigating concrete cracking issues. The new hybrid piers demonstrated safety factors greater than 2.4, and have been successfully applied in the background project.

KEYWORDS urban viaduct, hybrid pier, steel-concrete connection, hinged to rigid construction method, large-scale tests, finite element analysis

1 Introduction

Prefabricated bridge assembly technology has been widely applied in urban construction of small to medium-span bridges to accelerate construction procedure, reduce traffic interruptions, and minimize environmental impacts [1,2]. Typical prefabricated piers consist of precast concrete columns and cap beams. With the rising urban traffic demands, wide viaducts with eight or more vehicle lanes necessitate large-cantilevered cap beams in pier structures. In such applications, traditional precast concrete cap beams exhibited their limitations, such as massive volumes and heavy weights. For example, a precast concrete cap beam in an eight-lane bridge weighs approximately 400 t, posing challenges for transportation and assembly, as well as raising aesthetic concerns [3,4].

At present, three methods are applied to reduce the weight of prefabricated concrete cap beams. First,

Article history: Received Sep 15, 2025; Accepted Oct 26, 2025

optimized hollow sections are adopted instead of traditional solid section, such as inverted U-shape [5,6], inverted T-shape [7], box shape [8], and π-shape [9]. Although the weight of concrete cap beam can be reduced by 30%, they have lower bearing capacities and are prone to shear cracking and brittle failure [10]. Second, the concrete cap beam is prefabricated in segments and assembled on site. Studies on dry, wet, and adhesive joints between the segments [11–14] have found similar elastic behavior in both segmented and monolithic concrete cap beams. However, cracks typically initiate at the joints of segmented concrete cap beam in plastic phase, resulting in a 30% decrease in ultimate bearing capacity and poorer durability. In addition, semi-prefabricated cap beams with prefabricated shells and in situ cast concrete are compromised in the construction efficiency [15]. Finally, advanced construction materials such as ultra-high performance concrete (UHPC) and high-strength steel have been proposed for cap beams. The shear and bending performance of large-cantilevered thin-walled UHPC cap beams [9,16,17], semi-prefabricated UHPC formwork-reinforced concrete composite cap beam [18], and prefabricated high-strength steel-UHPC composite cap beams [3] have been studied through experiments and theoretical analysis. Although the self-weight of cap beams can be reduced by 40%, the high costs limit their wide applications.

To overcome the limitations of concrete cap beams, hybrid piers with steel cap beams and concrete columns have attracted attention as an alternative. In China, steel cap beams are predominantly used in portal piers of bridges spanning active railways [19], as the rapid construction method can minimize impact on railway traffic. Zhou [20] studied different cap beams in urban bridges and found that the weight of steel cap beams with the same bearing capacity was 68% of composite cap beams and 19% of concrete cap beams; meanwhile, the cost of substructure only increased by 6%, indicating the economic viability of steel cap beams. Meng et al. [21] found that filling the core area of box-shaped steel cap beam with concrete by half height of the cap beam significantly improved its stiffness and ultimate bearing capacity. In addition, Kitada et al. [22,23] verified through cyclic loading tests and pseudo-dynamic tests that using the techniques of concrete filling, stiffener strengthening and installing short segments improved the ductility, ultimate strength, and seismic performance of steel bridge piers. Shao et al. [3] manufactured two large-scale steel-UHPC composite cap beam specimens using high-strength steel and conventional mild steel; the four-point bending test results showed that the steel box and UHPC bottom slab of the composite cap beam were firmly connected and the relative interfacial slip was small, and the specimen made of high-strength steel exhibited a higher flexural capacity but lower ductility.

A critical aspect of the hybrid pier system is the connection between the steel cap beam and concrete column. To this end, research on similar steel-concrete joints in composite structures offer valuable reference. Yamada et al. [24] developed a joint structure in which steel beam flanges were welded with rebars and anchored in concrete columns. Nakamura et al. [25] proposed welding the steel beam and short transverse beam together to enclose the core concrete, and the structure exhibited sufficient plastic development and evenly distributed cracks in the concrete at failure. Matsui et al. [26] performed finite element (FE) analysis and showed that adding studs in the steel frame further strengthened the connection. Additionally, Suzuki et al. [27], Nishido and Nishido [28], Ji et al. [29], Liang et al. [30], and Xie et al. [31], etc. conducted experimental and numerical studies on local bearing connections, concrete-inserted connections, high-strength bolt connections, and optimized steel-sleeve connections.

In summary, to enable the rapid construction of urban viaducts, this study proposes a novel π-shaped hybrid pier with prefabricated large-cantilevered steel cap beam and concrete columns, based on the background project. The steel cap beam fully leverages the advantages of steel, including light weight, high strength, excellent ductility, and high factory prefabrication potential [32–34], thereby allowing for full-scale prefabrication and one-time hoisting. Furthermore, with considerations given to mechanical performance, construction efficiency and economic viability, two innovative connections are proposed: the flange-rebar-UHPC connection and the rebar-concrete connection.

Two large-scale (1:4) π-shaped hybrid pier specimens, based on the prototype piers in the background project, were fabricated in this study, using the flange-rebar-UHPC and rebar-concrete connections, respectively. A loading protocol simulating the actual loading conditions was adopted in the tests. The structural behaviors including ultimate bearing capacities, failure modes, strains and displacements of key sections were thoroughly analyzed. Subsequently, FE models were developed and validated using experimental results. FE parametric analysis was performed to further evaluate the influence from structural details of steel cap beams on the structural behavior. Furthermore, the influence of construction sequence was examined through FE analysis. Finally, the safety factors of the π-shaped hybrid piers were analyzed.

2 Conceptual design of π-shaped hybrid bridge piers

2.1 Background project

This study serves for a bridge project in Hangzhou,

Zhejiang Province, China, which is a supporting infrastructure for the Asian Games. The superstructure consists of four steel-concrete composite continuous girders with spans ranging from 33.5 to 40 m and a width of 25 m. Four bearings are arranged along the cap beam, one under each main girder, to transfer the loads from the superstructure to the pier, as shown in Fig. 1.

Fig. 1 The design of the background bridge.

2.2 Comparison of cap beams

Taking the substructure of six-lane bridge shown in Fig. 1 as an example, the conceptual design of the box-shaped steel cap beam is shown in Fig. 2(a). Specifically, a box-shaped steel cap beam (Fig. 2(b)), an inverted T-shaped steel cap beam (Fig. 2(c)), and a conventional box-shaped prestressed concrete cap beam (Fig. 2(d)), having the same bearing capacity, have been designed for comparison.

Table 1 makes a detailed comparison of the three cap beams in terms of materials, aesthetics, economy, self-weight, and construction. In Table 1, as the self-weight of the prestressed concrete cap beam is 291 t heavier than that of the box-shaped steel cap beam, an additional pile underground (diameter of 0.8 m; length of 50 m; bearing capacity of 300 t) is required to ensure the safety of the foundation, and the cost of a single pile is approximately 54350 yuan.

The total cost of a box-shaped steel cap beam is approximately 5% higher than that of a concrete cap beam. However, the steel cap beam exhibits a slightly slenderer appearance than concrete cap beams, and it weighs only 1/5 of that of concrete cap beams, facilitating transportation and hoisting. With minimal in situ assembly and concrete casting work, the construction time is significantly shortened, and the impacts on traffic and neighborhood are minimized. For infrastructure construction projects in busy metropolis, these factors are particularly important.

Importantly, Table 2 further compares the carbon emissions associated with different cap beams. According to the Standard for Calculation of Building Carbon Emissions (GB/T51366-2019) [36], the carbon emissions for only producing and transporting a concrete cap beam with an additional pile are estimated at about 207 t, while that for a steel cap beam is approximately 193 t, reduced by 7%. Furthermore, during the on-site construction, compared with the connection of steel structures via bolts and welding, the carbon emissions from hoisting heavy prefabricated concrete structures or casting concrete on site are much higher. Therefore, the steel cap beams offer a greener alternative, aligning with the goals of sustainable development.

In contrast, although the inverted T-shaped steel cap

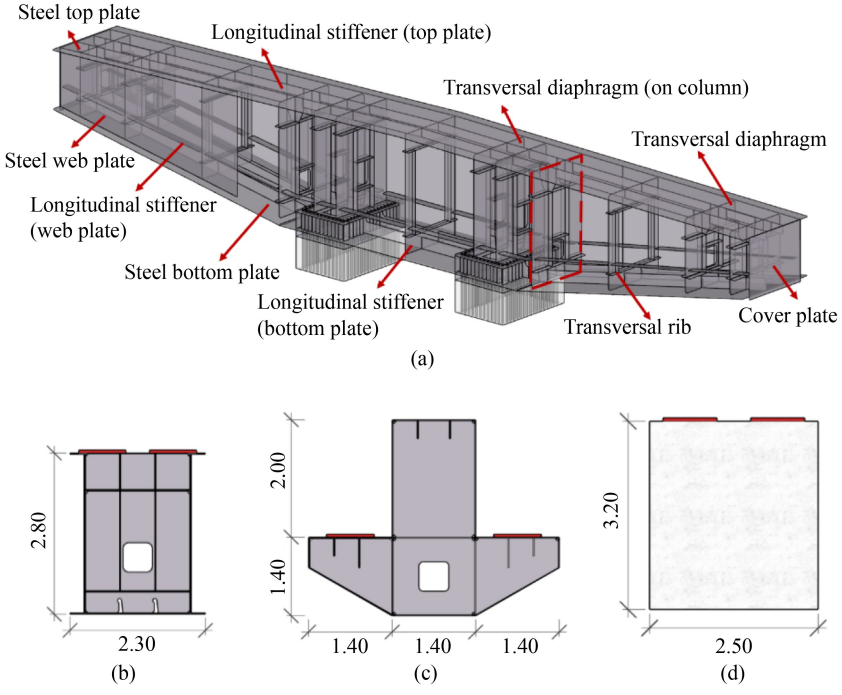

Fig. 2 The design of cap beams (unit: m): (a) overall design of steel cap beam; (b) box-shaped (steel); (c) inverted T-shaped (steel); (d) box-shaped (prestressed concrete).

Table 1 Comparison of technical and economic indexes*

Scheme	Height (m)	Cost of material				Cost of transportation and construction			Total cost (yuan)
		Material	Structure	Type	Quantity × unit price (Yuan)	Self-wight of cap beam (t)	Construction time (d)	Cost (Yuan)	
Box-shaped prestressed concrete cap beam	2.0–3.2	concrete	cap beam	C50 (m^3)	137 × 770 = 105490	356.2	10	84464	666412 (one extra pile for 54350, and management + tax for 138362)
			columns	C40 (m^3)	53 × 732 = 38796				
		rebar	cap beam	HRB400 (t)	16.9 × 4937 = 83603				
			columns	HRB400 (t)	24.5 × 4937 = 121149				
		steel strand	cap beam	15.2 (mm^2/t)	5.4 × 7403 = 40198				
Box-shaped steel cap beam	1.5–2.8	steel	cap beam	Q420q (t)	65.5 × 9069 = 594165	65.5	2	22268	902528 (management cost + tax for 145852)
		concrete	columns	C40 (m^3)	53 × 732 = 38796				
		rebar	columns	HRB400 (t)	16.7 × 4937 = 82236				
		UHPC	connection	C150 (m^3)	1.3 × 14778 = 19211				
Inverted T-shaped steel cap beam	3.0–3.4	the steel consumption is 85.2 t and other materials are almost the same as box-shaped steel cap beam, and the direct cost is 910978 yuan.				85	2	22268	1080778

*Note: The unit price adopts the guiding price of Shanghai, China (2020) [35].

Table 2 Comparison of carbon emissions

Scheme	Production stage				Transportation stage				Total (t)
	Material	Quantity	Carbon emissions	Total	Distance (km)	Quantity (t)	Carbon emissions (kg CO_2 e/(t·km))	Total (t)	
Box-shaped prestressed concrete cap beam	C40 concrete	53 m^3	340 kg CO_2 e/m^3	18 t	40	585	0.162	3.8	207
	C50 concrete	137 m^3	385 kg CO_2 e/m^3	53 t					
	concrete in pile	35 m^3	340 kg CO_2 e/m^3	12 t					
	steel rebar	41.4 t	2340 kg CO_2 e/t	97 t	500	50.3	0.057	1.4	
	prestressed tendons	5.4 t	2400 kg CO_2 e/t	13 t					
	rebar in pile	3.5 t	2340 kg CO_2 e/t	8 t					
Box-shaped steel cap beam	C40 concrete	53 m^3	340 kg CO_2 e/m^3	18 t	40	133	0.162	0.8	193
	UHPC	1.3 m^3	400 kg CO_2 e/m^3	0.5 t					
	steel	65 t	2050 kg CO_2 e/t	133 t	500	81.7	0.057	2.3	
	steel rebar	16.7 t	2340 kg CO_2 e/t	39 t					

beam has lower exposed height and greater stiffness, it involves more steel consumptions, complicated manufacturing, and inconvenient maintenance, thus its cost is much higher than that of box-shaped steel cap beams.

3 Specimens of the π-shaped hybrid bridge piers

Two large-scale (1:4) specimens of π-shaped hybrid bridge piers with large-cantilevered steel cap beams and concrete columns were fabricated, wherein specimen S1 adopted the flange-rebar-UHPC connection and specimen S2 used the rebar-concrete connection.

3.1 Specimen S1

3.1.1 The steel cap beam

The box-shaped steel cap beam in specimen S1 was welded using Q355 steel plates of different thicknesses, as shown in Fig. 3. Specifically, the total longitudinal length was 5390 mm, including the cantilever parts (1890 mm), the parts on columns (375 mm) and the part between columns (850 mm). The top plate had a 2% longitudinal slope, symmetric about the centerline. The height of web plate increased linearly from the cantilever end to the root, while the section between the columns maintained a constant height of approximately 700 mm. The widths of the top and bottom plates were 575 mm, and the distance between the webs was 450 mm. Such section design streamlined the load transfer from the superstructure to the piers as the web plates located underneath the bearings, and it also facilitated the flange-rebar-UHPC connection as detailed below.

The annotation format is "Name (Plate Thickness)", and the same applies hereinafter.

As shown in the sections A to D of Fig. 3, two longitudinal stiffeners were installed on each of the top

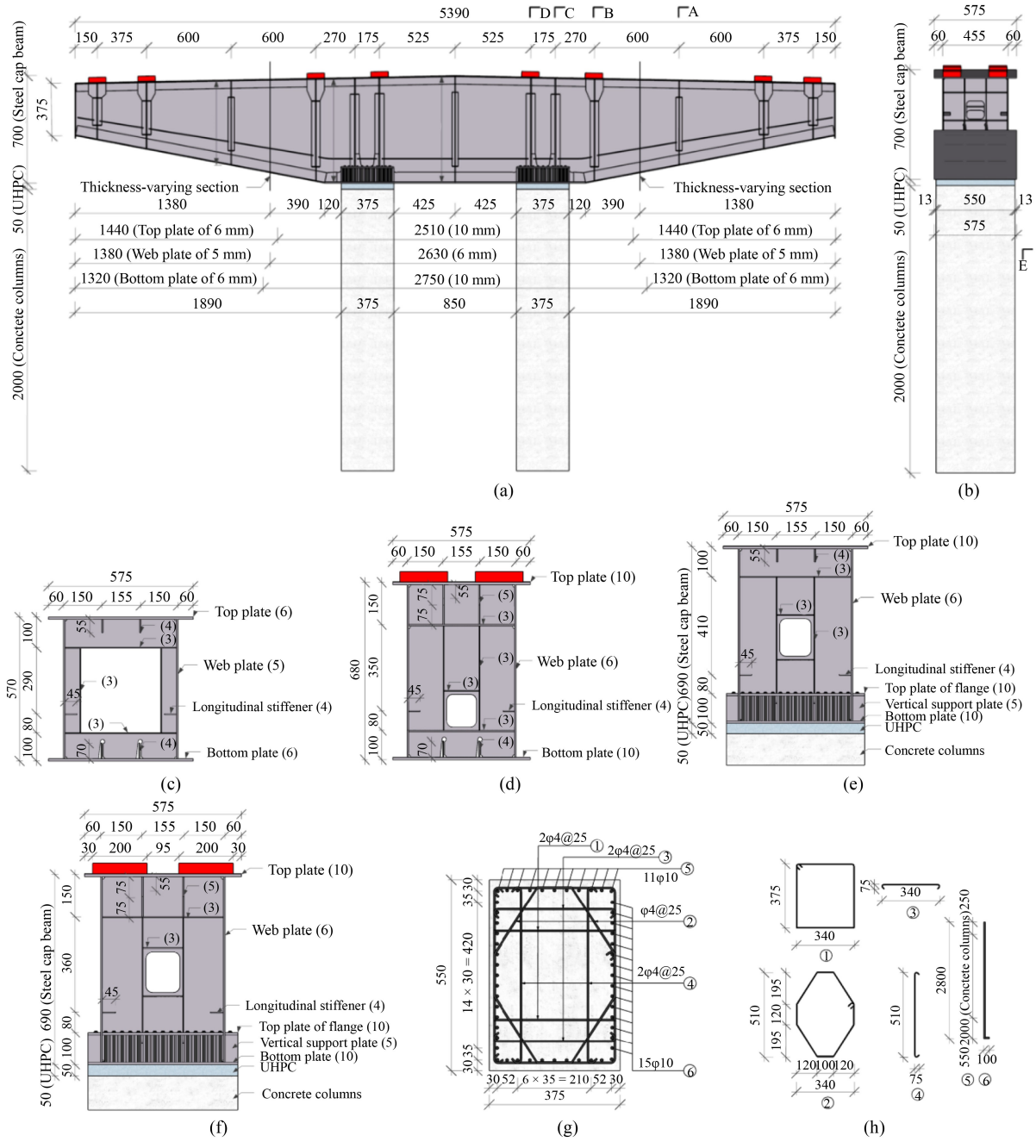

Fig. 3 The design of specimen S1 (unit: mm): (a) front view; (b) side view; (c) section A; (d) section B; (e) section C; (f) section D; (g) section E; (h) rebars.

plate, web plate, and bottom plate of steel cap beam, to improve stiffness and buckling resistance. Three transverse stiffeners were located at the plate thickness-varying sections and the centerline section. Ten transverse diaphragms were set at sections under the bearings or above the concrete columns to transfer loads and enhance the overall stiffness.

Notably, the varied plate thickness design of steel cap beam was crucial for fully utilizing the steel strength and reducing steel consumption. The loads from the superstructure were concentrated on each bearing, leading to step-shaped distributions of shear forces and bending moments on steel cap beam, and both reached the maximum at section B in Fig. 3. Therefore, the thickness-varying section was positioned between sections A and B of the cantilever part. By using thinner steel plates near the cantilever ends and thicker plates near the root, the stress levels at the different sections were controlled to be comparable. To ensure smooth plate thickness transition, the welds between plates of different thicknesses at the top, web, and bottom plates were staggered by 60 mm.

3.1.2 The concrete column

The concrete column of specimen S1 had a height of 2000 mm, and with a rectangular cross-section measuring 550 mm × 375 mm, as shown in Fig. 3(c). The rebar framework of the column was assembled using HRB400 rebars. Specifically, 10 mm diameter vertical rebars were arranged in both longitudinal (⑤) and transverse (⑥) directions, with a total length of 2800 mm, including a 250 mm at the top for connection and a 550 mm embedded in the foundation. The tensile rebars (③ and ④), rectangular stirrups (①), and diamond stirrups (②) in the horizontal sections all had a diameter of 4 mm, to fix the vertical rebars and confine concrete. The concrete columns of the specimens were cast on site using C40 concrete with fine aggregate; Nevertheless, the concrete columns in the background project were assembled by precast concrete segments.

3.1.3 The flange-rebar-ultra high performance concrete connection

An innovative flange-rebar-UHPC connection along with a unique construction method was proposed as shown in Figs. 4(a) and 4(b). The construction sequence for application in actual bridge piers is as follows. First, laminated rubber bearings are placed on top of cured concrete columns. Subsequently, the steel cap beam is placed onto the laminated rubber bearings, with the rebars passing through the flange plates of steel cap beam. Bolts are initially screwed to prevent the steel cap beam from overturning. Thereafter, four main girders are installed in a symmetric order onto their respective bearings from the inner to the outer sides. After the substructure has experienced deformations under the self-weight of main girders, all bolts are fully tightened and UHPC between the bottom plate of steel cap beam and concrete column is cast. Finally, the bridge deck pavement, rails, and other ancillary components are constructed.

The advantages of the flange-rebar-UHPC connection are its convenience and rapidity for construction. Specifically, upon the completion of concrete columns, the installation of the steel cap beams and main girders can be finished within two days, which significantly shortens the construction time. Additionally, this innovative construction can also benefit the stress distributions of the concrete columns by reducing the bending moments caused by the self-weight of the superstructure and using UHPC (as detailed in Subsection 6.4).

However, the construction sequence of specimen S1 was modified as follows, because the 1:4 scaled specimen had inadequate internal space for personnel to enter, while some bolts for the flange connection need to be tightened inside the steel cap beams (in contrast, the internal space of the actual steel cap beams is accessible for manual operations). Therefore, the steel cap beam of specimen S1 was divided into five segments. The segments on columns were installed and the bolts inside web plates were tightened first. Then, the other segments

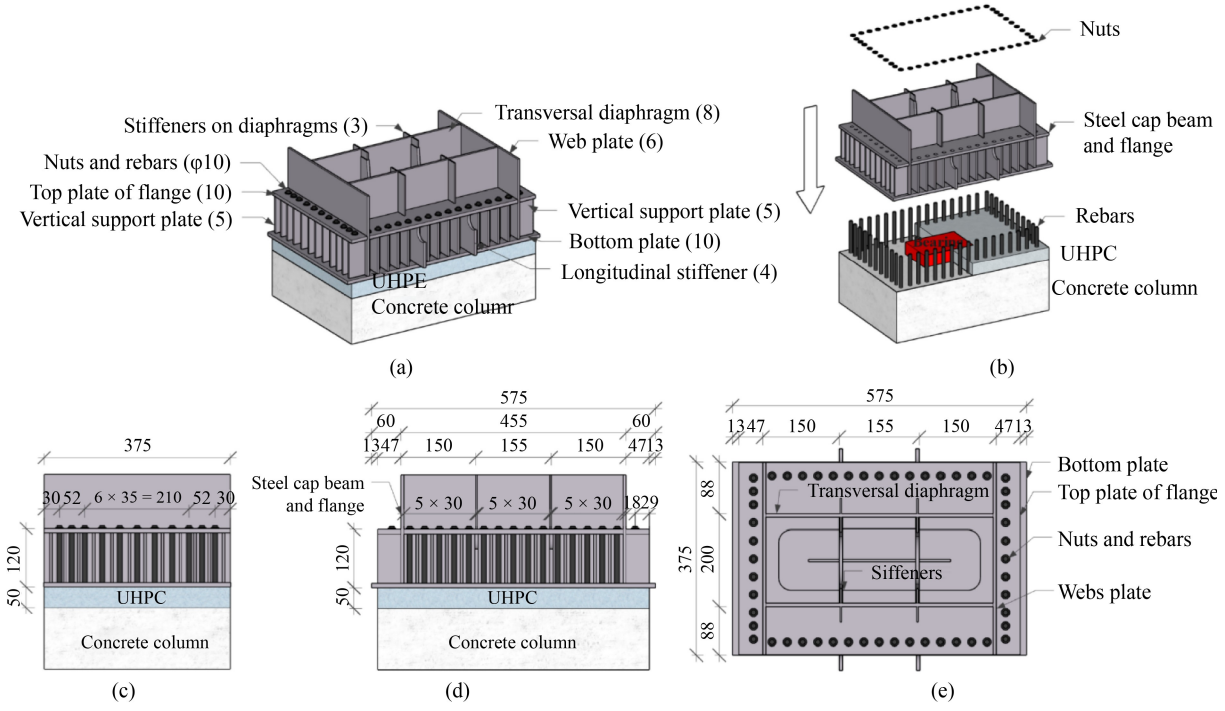

Fig. 4 The flange-rebar-UHPC connection (unit: mm): (a) overall design; (b) construction method; (c) side view; (d) front view; (e) plan view.

were welded to form the complete steel cap beam. Finally, UHPC was cast and the bolts outside the web plates were tightened.

3.2 Specimen S2

The steel cap beam of specimen S2 is shown in Fig. 5(a). Different from specimen S1, the spacing between webs was 550 mm, consistent with the transverse width of the concrete column. The detailed design of the rebar-concrete connection is shown in Figs. 5(b)−5(f). Horizontal and vertical perforated plates were set at the webs and transverse diaphragms, to anchor the vertical and transverse short rebars in concrete columns, respectively.

In actual projects, the transverse short rebars are first fixed to the perforated plates inside the steel box chamber. Then, as vertical rebars pass through the bottom plate and horizontal perforated plates, the steel cap beam is placed on the laminated rubber bearing at the top of concrete columns. After the steel sleeves are welded between the bottom plate of steel cap beam and concrete column, C40 concrete is poured from the top plate until filling the entire joint section. However, in the test, it was difficult for rebars to pass through the perforated plates due to limited internal spaces of the 1:4 specimen. Therefore, the horizontal perforated plates and transverse rebars were removed in specimen S2.

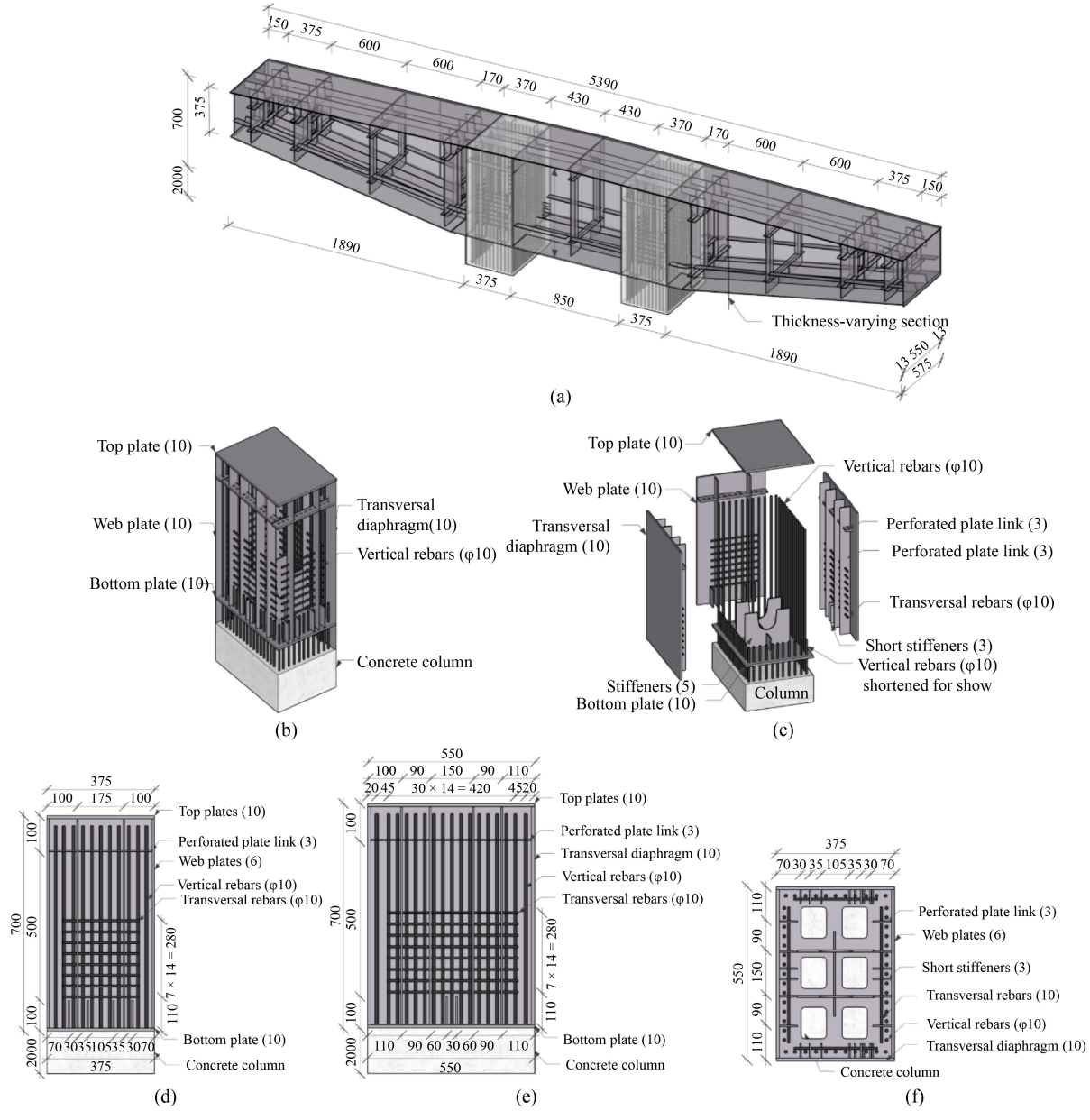

Fig. 5 The rebar-concrete connection (unit: mm): (a) the steel cap beam of specimen S2; (b) overall design; (c) construction; (d) side view; (e) front view; (f) plan view.

For this rebar-concrete joint, one of the difficulties during construction is fixing the transverse short rebars to perforated plates, and accurately passing vertical rebars through the holes in bottom plate and perforated plates within the complex steel box chamber. This puts high accuracy demands for fabrication and construction. In addition, each joint requires approximately 10 m^3 of concrete casting on site. However, the rebar-concrete joints are expected to have high stiffness and capacity (the joint section is equivalent to an extension of concrete column), such that the rotation and displacement of the cantilever beam can be reduced.

3.3 The fabrication of specimens

The fabrication process of specimen S1 and S2 is shown in Fig. 6. The parts Figs. 6(a)−6(d) are the same for both specimens.

4 Test program

4.1 Loading system

The test utilized a self-reaction system as shown in Fig. 7. Four individually controllable jacks were placed at the bearing positions on top of steel cap beam. Each jack was attached to a stiff transverse distribution beam above them, which were connected to the strong steel base by prestressed steel tendons. The steel tendons were properly aligned and tensioned to ensure accurate and stable load application by the jacks.

4.2 Loading protocol

A loading protocol as shown in Table 3 was adopted. A symmetric loading configuration was adopted in the test. Specifically, the outer loads (Load ① and ④ in Fig. 7) applied equally, and the inner loads (Load ② and ③) were equal, but the outer and inner loads could be different. Both specimens S1 and S2 subjected to a consistent loading protocol.

The loading process was divided into five steps. In the pre-loading step, four jacks were slowly loaded to 40 kN and then unloaded, to ensure the normal functioning of the equipment. Step 1 simulated the self-weight of the main girders (P_w), corresponding to 148 kN for each jack. Step 2 simulated the load of serviceability limit state, including additional loads from the weight of auxiliary structures (60 kN for each jack) and the vehicle loads. According to the General Specifications for Design of Highway Bridge and Culvert (JTG D60-2015) [37], the bending moment at the top of concrete column in the background bridge under the most unfavorable vehicle load is 13600 kN·m, and the vertical axial force is 2500 kN, which are equivalent to 212 kN·m and 156 kN in the 1:4 scaled specimen. Conservatively, since the minimum distance from the outer bearing to concrete

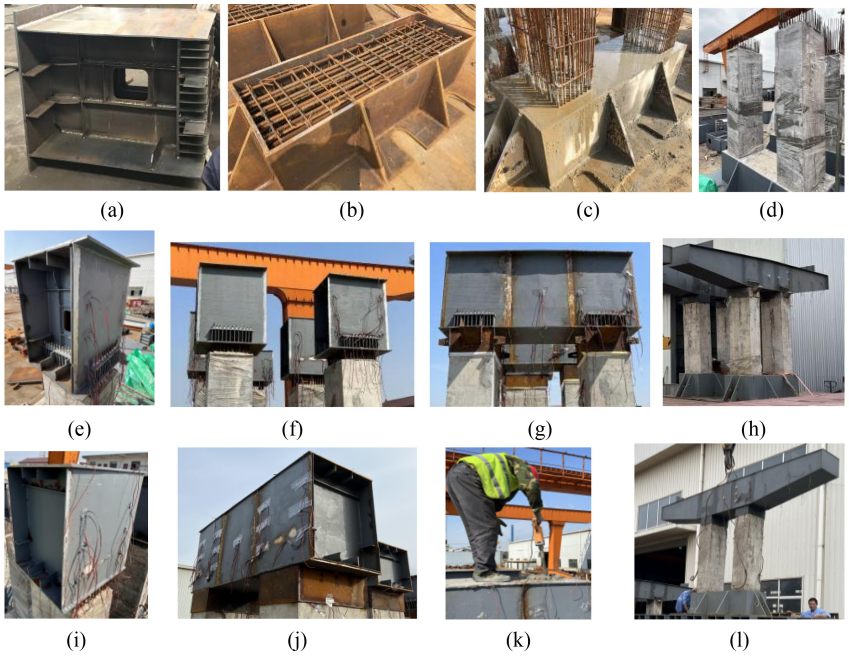

Fig. 6 The fabrication process of specimens: (a) fabrication of steel cap beam segments by welding steel plates; (b) the rebar framework of the concrete foundation; (c) the rebar framework of the concrete column and the cast concrete of the foundation; (d) concrete casting of the columns. Specimen S1: (e) installation of the cap beam–column joint segment with the bolts between the webs tightened; (f) installation of two joint segments; (g) welding of the segments between columns, casting of UHPC, and tightening of bolts on the outer sides of webs; (h) The complete specimen S1. Specimen S2: (i) installation of the cap beam–column joint segment; (j) welding of the segments between columns; (k) casting of the concrete at the joints; (l) the complete specimen S2.

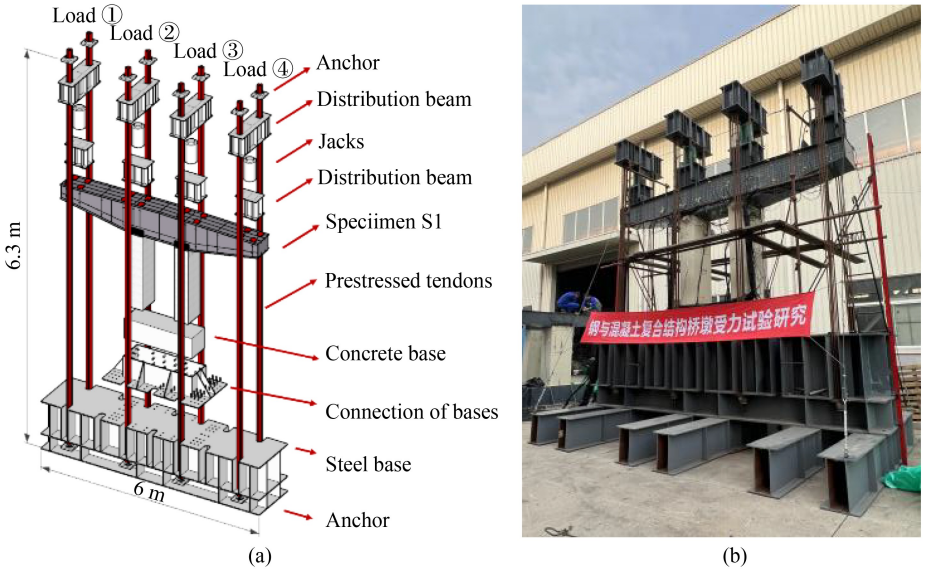

Fig. 7 Loading system (specimen S1): (a) design; (b) on testing site.

Table 3 Steps of the test

Step	Outer load (kN)	Inner load (kN)	Remark
0	40	40	pre-loading
1	148	148	P_w: self-weight of the main girders
2	364	208	P_s: the load of serviceability limit state
3	740	432	P_e: the structural elastic limit capacity
4	+17 kN / time till failure	+10 kN / time till failure	P_u: the ultimate bearing capacity of the hybrid pier

column is 1.37 m (Fig. 5(a)), the bending moment at the top of concrete column is 213 kN·m when the outer load is 156 kN. Thus, the total outer load was designed as 148 kN + 60 kN + 156 kN = 364 kN and the inner load was 148 kN + 60 kN = 208 kN in Step 2.

Step 3 was designed to reach the structural elastic limit capacity, based on calculations using the measured material properties as introduced in the following subsection. The loadings in steps 1, 2, and 3 were applied in 5, 10, and 20 equal load increments, respectively. Measurements were recorded when the load stabilized after each increment. In Step 4, the structure was loaded with the increments as detailed in Table 3 until failure.

4.3 Test of material properties

Tables 4 and 5 summarize the experimentally measured material properties of steel, concrete and UHPC, and the results are the average value of three repetitive tests.

Specifically, the tensile test of steel plate was carried out according to the Metallic Materials-Tensile Testing (GB/T 228.1-2021) [38], and the elastic modulus was taken as 206 GPa in accordance with the Code for Design of Steel Structures (GB50017-2017) [39].

According to the Standard for Test Methods of Physical and Mechanical Properties of Concrete (GB/T 50081-2019) [40], the compressive strength, flexural strength, tensile strength, and elastic modulus of concrete used in columns and connections were tested through cubic, prismatic, or dog-bone-shapes samples, respectively. It should be noted that, consistent with the design of actual structure, C40 concrete was planned for the scaled model test. While the mix proportion of the concrete should be correct, the on-site pouring construction was carried out in an outdoor site in winter. Therefore, the pouring and curing processes of the concrete might cause its lower strength to the grade. However, the material properties of this concrete were measured from actual tests, and the data were used in the following tests and FE analyses. In addition, the UHPC in test was mainly composed of powder, steel fibers and water, in a proportion of approximately 25:2.3:2.5, and the average length of steel fibers was about 16 mm to ensure the tensile strength.

4.4 Instrumentations

The real-time measurements, including loads, strains, and displacements of key sections, were recorded in the tests. The instrumentation layout for specimen s1 is shown in Fig. 8, and specimen S2 adopted a similar layout except for the joint zone. Strain gauges were mounted on Sections 1 to 11 of the steel cap beams and on Sections 12 to 17 within the joint zones and concrete columns. In addition, displacement transducers were deployed at

Table 4 Material properties of Q355 steel

Designed/real thickness (mm)	Position	Yield strength (MPa)	Ultimate strength (MPa)	Ultimate strain ($\times 10^{-6}$)
3/2.69	local stiffeners	477	582	132600
4/3.62	transverse diaphragms and ribs	419	566	137000
5/4.59	longitudinal stiffeners/web	423	553	136000
6/5.50	top and bottom plates/web	474	634	111000
8/7.60	longitudinal stiffeners	411	578	136300
10/9.55	top and bottom plates/flange	443	615	103000

Table 5 Material properties of concrete

Concrete	Position	Size (mm)	Test content	Test result (MPa)
C40	columns of S1 and S2	150 × 150 × 150	compressive strength	27.5
		150 × 150 × 150	flexural strength	5.1
	connection joint of S2	150 × 150 × 150	compressive strength	31.7
UHPC	connection joint of S1	100 × 100 × 100	compressive strength	150.4
		100 × 100 × 300	flexural strength	139.0
		100 × 100 × 300	elastic modulus	47700
		dog-bone	tensile strength	14.2

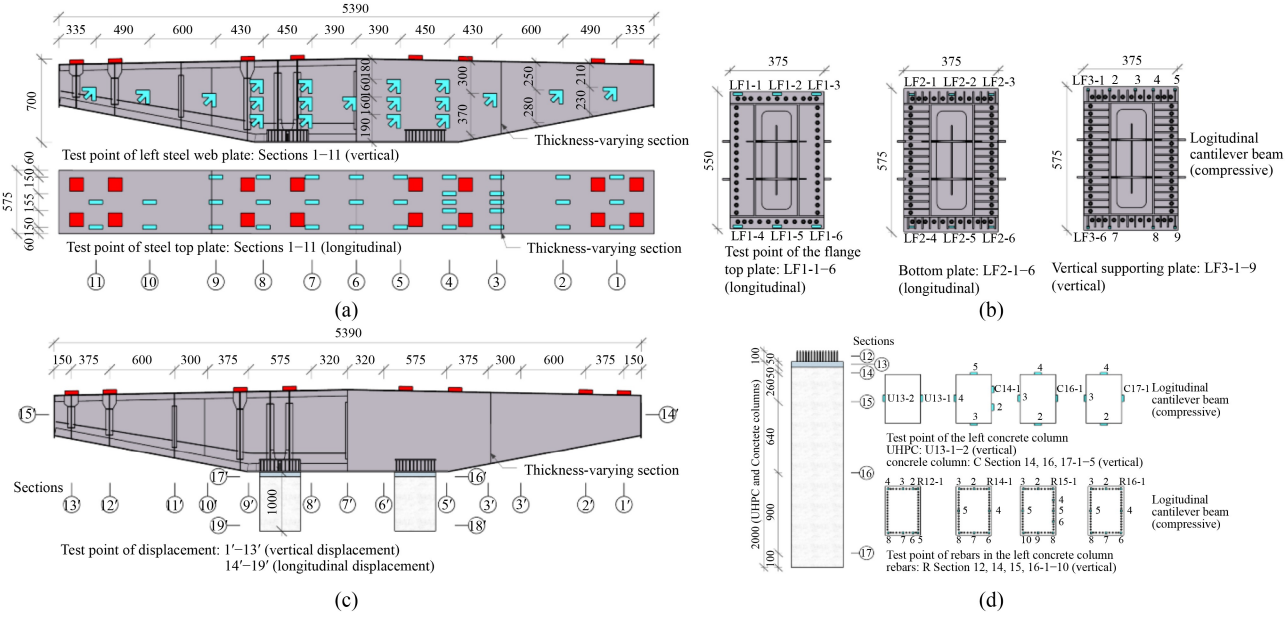

Fig. 8 Instrumentation layout (unit: mm): (a) the strain gauges on steel cap beam; (b) the strain gauges on joint; (c) the displacement transducers at sections 1′ to 19′; (d) the strain gauges on concrete column.

sections 1′ to 13′ along the steel cap beam to measure the vertical displacements and at sections 14′ to 19′ for the horizontal displacements.

The loads were measured through the oil pressure of the hydraulic jacks, which was calibrated before the testing. The horizontal and vertical displacements were measured by wire-drawing displacement transducers. Three types of strain gauges were pasted on the polished surfaces of the specimens. Short unidirectional strain gauges for steel were attached to most of steel plates and rebars, while triaxial strain rosettes (45°) were arranged on the webs of steel cap beams for measuring their principal stress. Additionally, long unidirectional strain gauges for concrete were mounted on the surfaces of the concrete and UHPC. Finally, estimated by the FE method, the rigidity of the steel base was so high that its vertical displacement during the test was less than 1% of the ultimate displacement of steel cap beam, and no correction was needed for the displacement measurement.

5 Test results and discussions

5.1 Experimental phenomenon and failure mode

5.1.1 Specimen S1

The phenomena of specimen S1 at different phases in test were as follows. 1) The π-shaped hybrid pier was in the elastic phase during loading steps 1 to 3. The cantilever beam of steel cap beam deformed with a constant stiffness under the combined action of bending moment and shear force. The cantilever root section exhibited the maximum longitudinal strain. 2) When the outer loads (Load ① & ④) were 939 kN in step 4, the longitudinal compressive strain of the bottom plate at cantilever root first reached the yield strain of 2106×10^{-6}. As the load increased, the top and web plates at root section yielded successively, and the yielded area gradually expanded. The stiffness of cantilever beam gradually decreased. 3) Finally, when the outer loads and inner loads were 1023 and 592 kN, respectively, a loud sound occurred inside the steel cap beam. The cantilever ends exhibited obvious downward displacements, and significant local buckling appeared on the web and bottom plates in the middle of cantilever beam, as shown in Fig. 9.

The failure mode of specimen S1 was primarily local buckling at the web and bottom plates of the cantilever part of the steel cap beam, as shown in Fig. 9(a). In Fig. 9(b), Buckling 1 referred to the inward deformation of lower web near the diagonal line (approximately 60°) between thickness-varying section and transverse rib. Similarly, Buckling 3 was caused by the principal stress occurred at the same position of the web on the other side. In addition, between Buckling 1 and Buckling 3, the bottom plate below transverse rib experienced severe deformation due to longitudinal compressive stress, which interacted with the local buckling of web plates.

In Fig. 9(c), Buckling 2 occurred at web near the diagonal line (approximately 45°) between the transverse diaphragm and rib under the outer bearing. Both web plates at Buckling 2 and 3 deformed inward, while the web plate between them deformed outward. In addition, Buckling 4 occurred at a symmetric position to Buckling 2 about the centerline, exhibiting smaller deformation.

Furthermore, in accordance with the Code for Design of Steel Structures (GB 50017-2017) [39], the limit of

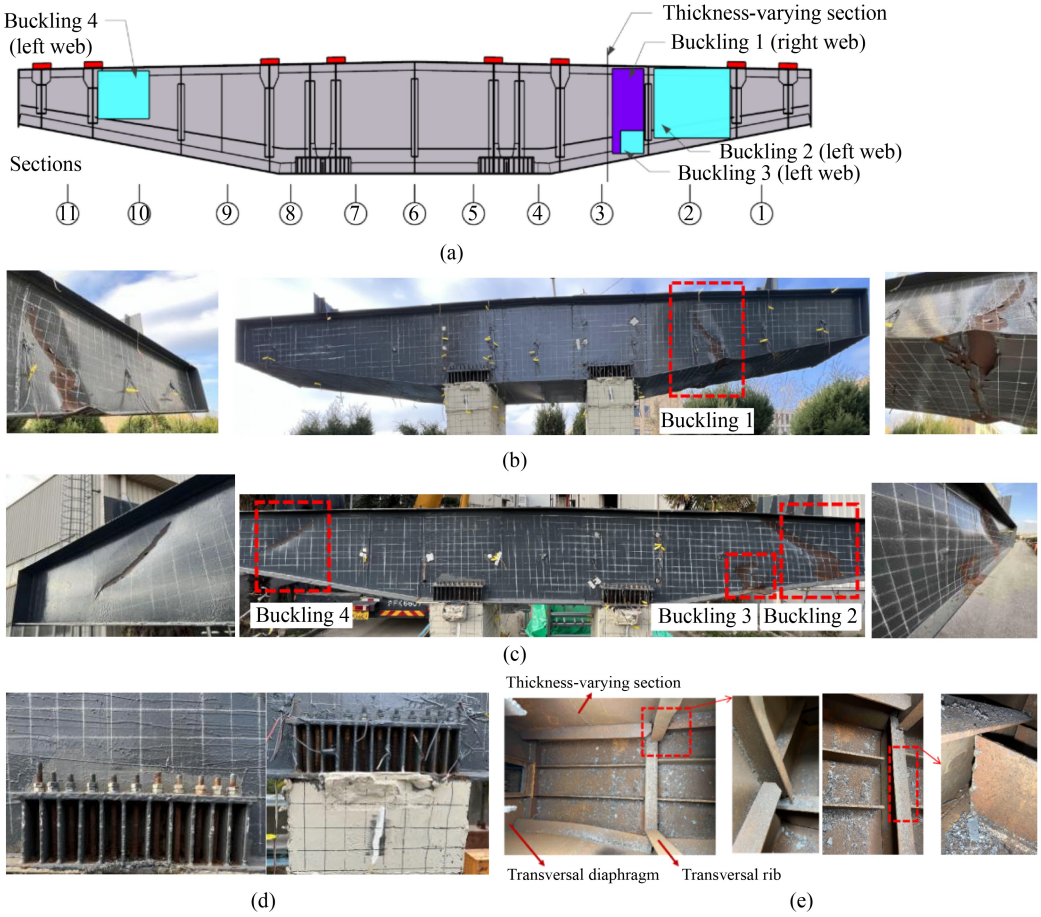

Fig. 9 The failure mode of specimen S1: (a) the positions of local buckling; (b) Buckling 1; (c) Buckling 2, 3, and 4; (d) the flange-rebar-UHPC connection; (e) the interior of steel cap beam.

elastoplastic shear buckling stress for the webs where local Buckling 1 and 3 occurred was 145 MPa, while that for the webs of local Buckling 2 and 4 was 177 MPa. In the test, the shear strain of the webs at corresponding positions was about 300 MPa which significantly higher than these limits, leading to the occurrence of local buckling.

In Fig. 9(d), upon inspection, no damage was identified for the flange of the steel-concrete joint. Meanwhile, no crushing or tensile cracking occurred at the UHPC or concrete columns.

Finally, after cutting off the top plate of steel cap beam, the buckling deformation of the lower webs near transverse rib was inspected from inside, as shown in Fig. 9(e). At this location, it was found that the longitudinal stiffeners of bottom and web plates were disconnected at the transverse diaphragms and ribs, and the welds between transverse rib and bottom plate was incomplete and broken. These were identified as structural detailing defects (they were supposed to be connected). These defects reduced the local stiffness at the transverse rib of steel cap beam, induced local buckling and affected the ultimate state of steel cap beam (the influence was further quantified in Subsection 6.3).

5.1.2 Specimen S2

The phenomena and failure modes of specimen S2 in the test were similar to specimen S1, as shown in Fig. 10. When the outer loads were 680 kN, the longitudinal tensile strain of the top plate at Section ③ first reached yield strain of 2160 με. Finally, the steel cap beam failed when the outer loads and inner loads were 878 and 515 kN. The lower webs on both sides of cantilever beam near the transverse ribs deformed inward along the diagonal direction (local Buckling 1 and 2). Meanwhile, the bottom plate below transverse ribs experienced severe deformation and buckling. After cutting off the top plate, the same defects as specimen S1 in steel cap beam were observed.

5.2 Load-displacement response

Figure 11 shows the comparison of load−displacement

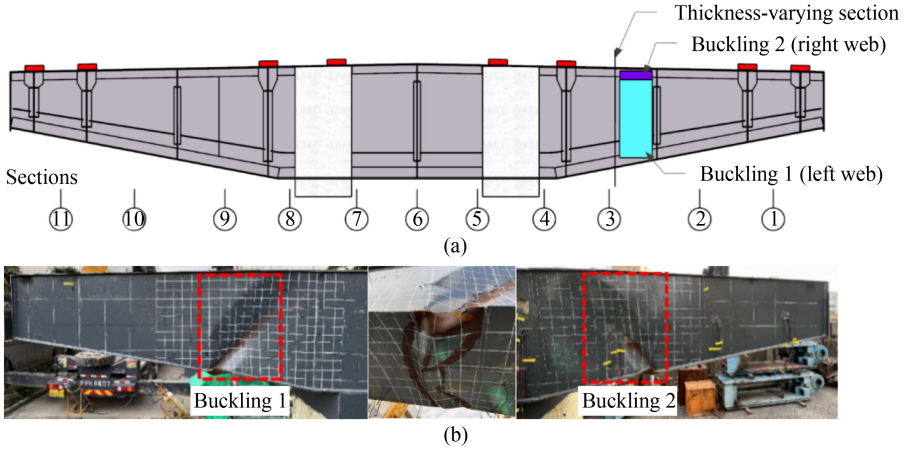

Fig. 10 The failure mode of Specimen S2: (a) the positions of local buckling; (b) Buckling 1 and 2.

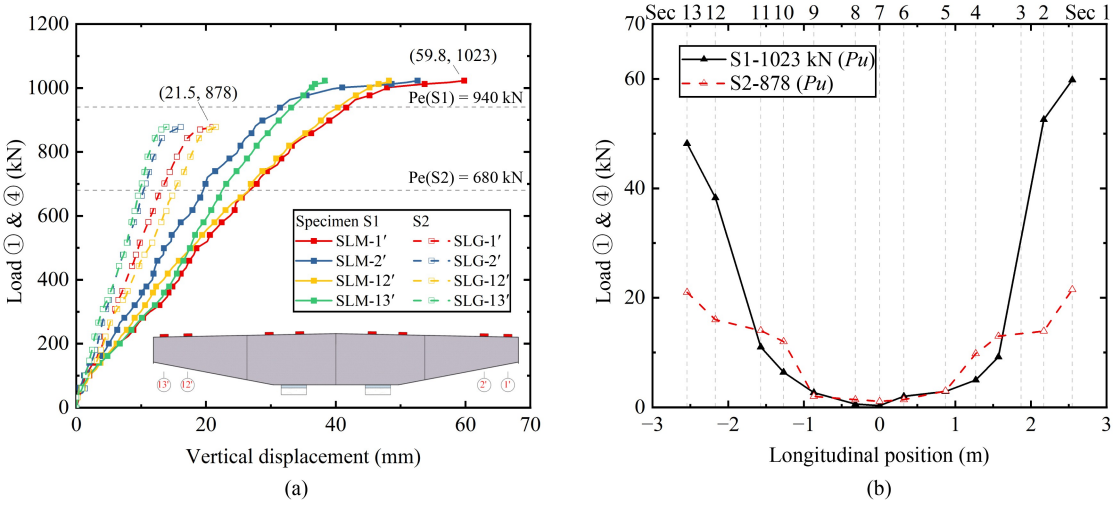

Fig. 11 The comparison of load–displacement of specimens S1 and S2: (a) load–displacement curve; (b) displacement along specimens.

curves of specimens S1 and S2, and the following observations were drawn. 1) In the elastic phase, the displacements of cantilever beams on both sides were basically symmetric, while that of specimen S1 was larger at corresponding sections under the same load. 2) In the plastic phase, the vertical displacements of specimens S1 and S2 increased rapidly. 3) At the ultimate phase, the vertical displacements at the cantilever ends of specimens S1 and S2 were 59.8 and 21.5 mm, respectively, corresponding to approximately 1/30 and 1/83 of the cantilever length. This indicated that both Specimens S1 and S2 had good deformation capacity, while the smaller displacement of specimen S2 was attributed to the more stiff cap beam–column joint which limited the rotation angle and displacements. 4) A significant overall downward displacement was observed at the end Section 1′–2′ of specimen S1, whereas specimen S2 exhibited a more evenly distributed displacement pattern. This might be attributed to the bigger web spacing of S2, which allowed the loads diffuse during transmitted to the webs and bottom plate through the transverse diaphragms and stiffeners. In contrast, the webs of S1 were exactly located under the support, thus directly bearing the shear force without diffusion, leading to overall deflection.

5.3 Load–strain response

5.3.1 The steel cap beam

The strains of cantilever beams on both sides were basically symmetric due to the loading scheme, thus taking one side as an example. The load–strain curves of specimen S1 and S2 are shown in Figs. 12 and 13. Herein, the strain was the max of values measured at the same section. The tensile strain was positive and the compressive strain was negative.

The figures indicated that: 1) in the elastic phase, the strains of top and bottom plates increased linearly; 2) in the plastic phase, when the outer loads of specimen S1 were 940 kN, the bottom plate of Section ④ yielded first, and when that of specimen S2 was 680 kN, the top plate of Section ③ yielded first. Subsequently, the longitudinal strains of both specimens increased more rapidly. 3) At the ultimate phase, the maximum longitudinal tensile strains of the top plate were both at Section ③, while the

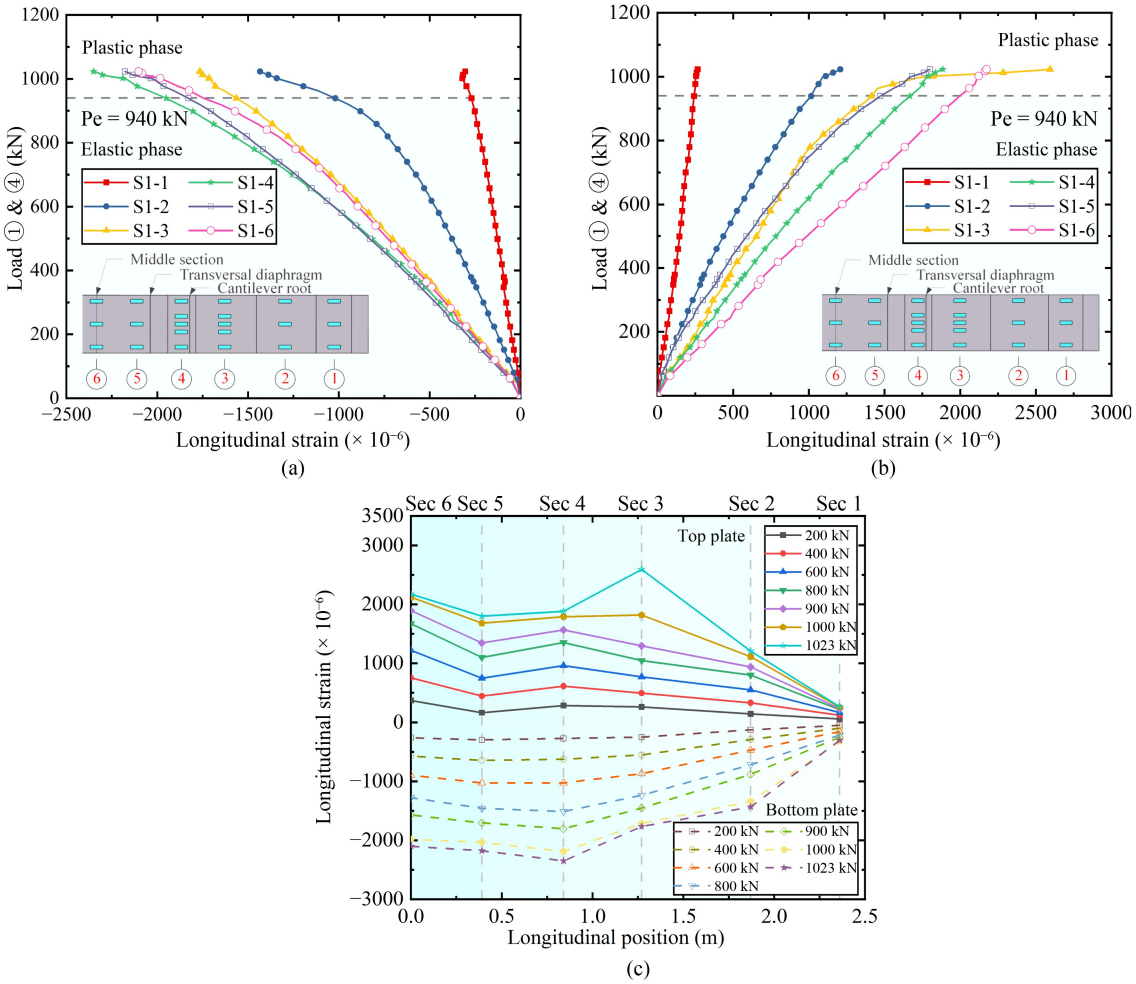

Fig. 12 Load–strain curve of specimen S1: (a) the bottom plate; (b) the top plate; (c) strain along cantilever beam.

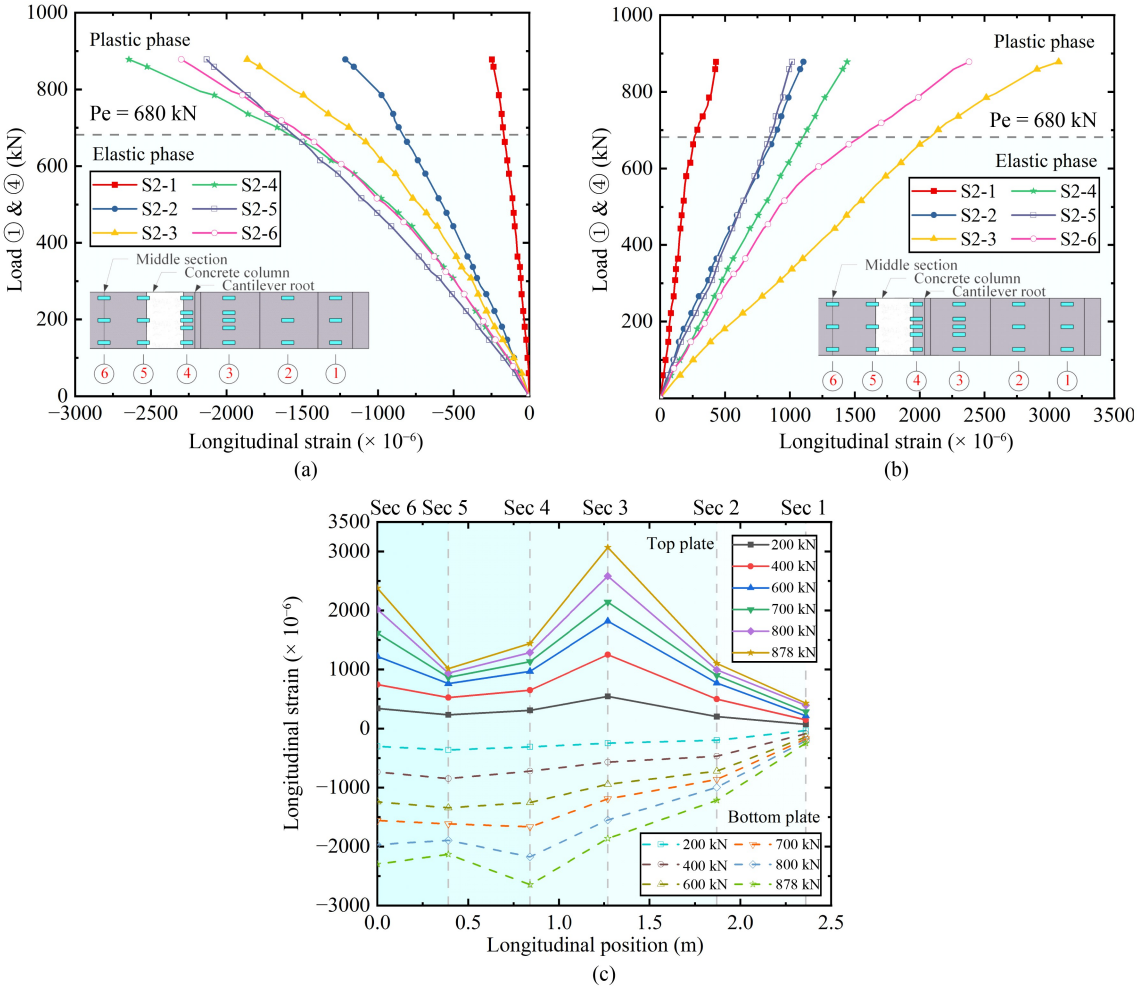

Fig. 13 Load–strain curve of specimen S2: (a) the bottom plate; (b) the top plate; (c) strain along cantilever beam.

maximum longitudinal compressive strains were both at Section ④. Meanwhile, the strains of middle sections were also large. 4) Overall, the longitudinal strains of bottom plates between Sections ① and ④ of two specimens gradually increased from the end to the root of cantilever beam, while the longitudinal tensile strain of the top plate at Section ③ was the largest. The reason could be that the plates from Section ① to ③ was thinner while that from Section ④ to ⑥ was thicker, which illustrated that the design of variable thickness could make full use of steel plate strengths. 5) specimen S2 failed at Section ③ where the tensile strain of the top plate increased the fastest. In contrast, the tensile strains of the top plates at Sections ④ and ⑤ increased slowly. This was attributed to that the strain gauges on the top plates of these two sections were close to the joint filled with concrete, whose large stiffness led to small longitudinal strains and rotation angles.

5.3.2 The flange-rebar-ultra high performance concrete connection

For the joint of specimen S1, the load–strain curves of the flange, UHPC, and rebars (Sec 12) are shown in Fig. 14. Taking the left column (L) as an example, some missing test data are supplemented with that of the right column (R). The side of the joint close to cantilever beam is designated as Side C, and the other side is Side T.

Figure 14 indicates that: 1) the flange-rebar-UHPC connection was in the state of small eccentric compression, and while Side C was under vertical compression, Side T was in tension; 2) when the steel cap beam failed, the flange remained in the elastic phase, consistent with the fact that no visible deformation and failure were observed in the test; 3) affected by the webs and transverse diaphragms that mainly transmitting forces, the longitudinal strain distributions of the top and bottom plates on flange were opposite and complex, as the top plate was slightly compressed on Side C and in tension on Side T; 4) both the UHPC and rebars were in eccentric compression. Although the maximum compressive and tensile strains on the surface of UHPC were 463×10^{-6} and 894×10^{-6}, no visible cracks were observed, though some micro-cracks might exist as detected by the 10 cm long strain gauges.

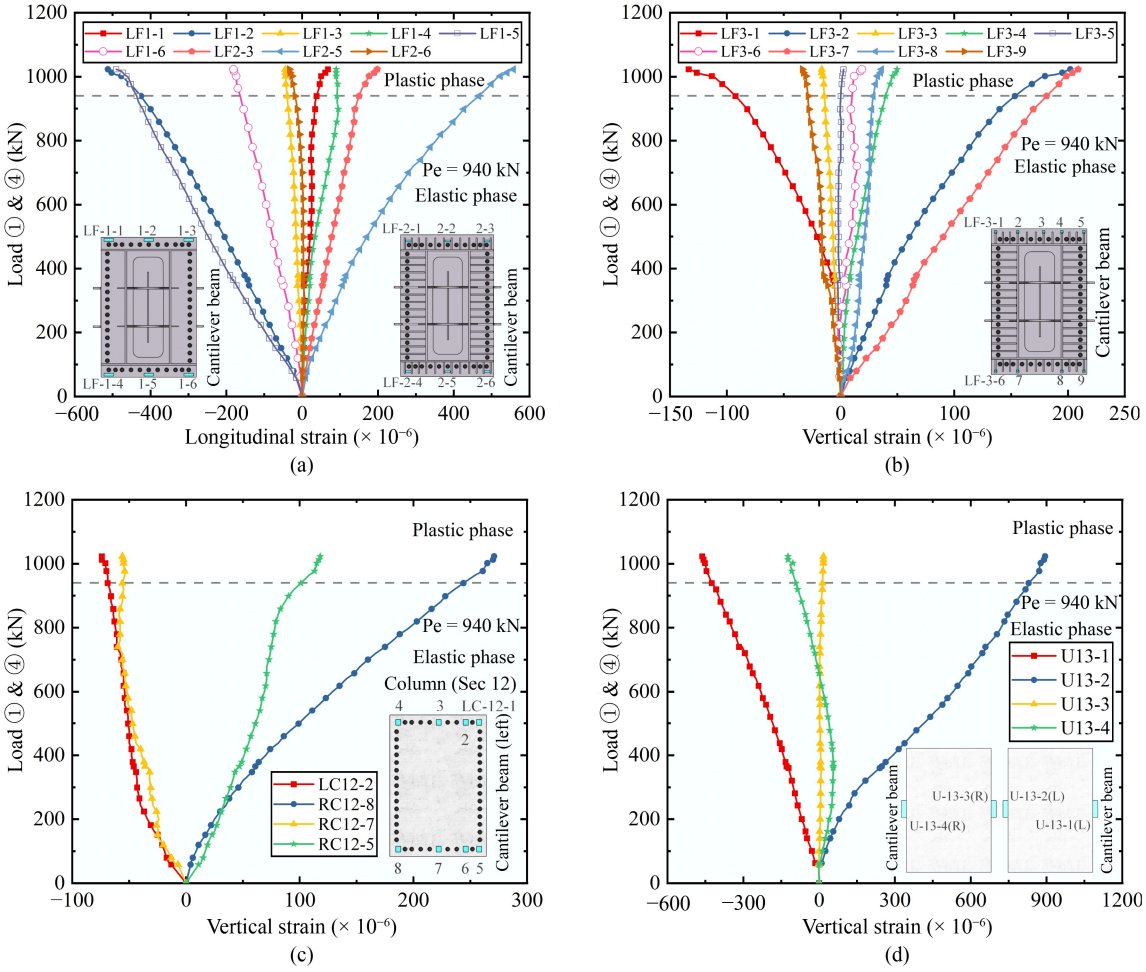

Fig. 14 Load–strain curve of the flange-rebar-UHPC connection: (a) the top and bottom plate of the flange; (b) the vertical support plate; (c) the rebars; (d) the UHPC.

5.3.3 The rebar-concrete connection

The monitored sections of specimen S2 are shown in Fig. 15(a), and the load–strain curves of the rebar are shown in Figs. 15(b)–15(d). Figure 15 exhibits that: 1) the rebar-concrete connection was under small eccentric compression, and while the rebars on Side C close to the cantilever beam was obviously under vertical compression, Side T was slightly in tension; 2) when the steel cap beam failed, the strains of the rebars in Section 12 and Section 13 were both in the elastic phase. Meanwhile, the compressive strain of the rebars on Side C of Section 14 was close to the elastic limit.

5.3.4 The concrete columns and rebars

Figures 16 and 17 exhibit the vertical strains of the rebars and concrete along the columns for specimens S1 and S2 under different loads. The figures indicate that, the rebars and concrete of two specimens deform coordinately and bear forces together, with the overall structural behavior characterized by eccentric compression.

Moreover, when the Specimen S1 and S2 failed, the rebars were still in the elastic phase. The maximum compressive strain of rebars in S1 was 1100 $\times 10^{-6}$ at Section 15 (360 mm below the bottom plate), and that in S2 was 1675 $\times 10^{-6}$ at Section 14 (60 mm below the bottom plate). Therefore, it is recommended that the anchorage length of rebars should be greater than 1 m (100 times the diameter of rebars), and at least 400 mm (40 times the diameter of rebars).

6 Finite element analysis

6.1 Finite element models

To further investigate the structural behavior of the π-shaped hybrid piers, three-dimensional FE models of the piers were established using ANSYS software, as shown in Fig. 18. In the FE model, the shell181 elements, solid65 elements, and link8 elements were used to simulate the steel cap beam, concrete columns, and rebars, respectively.

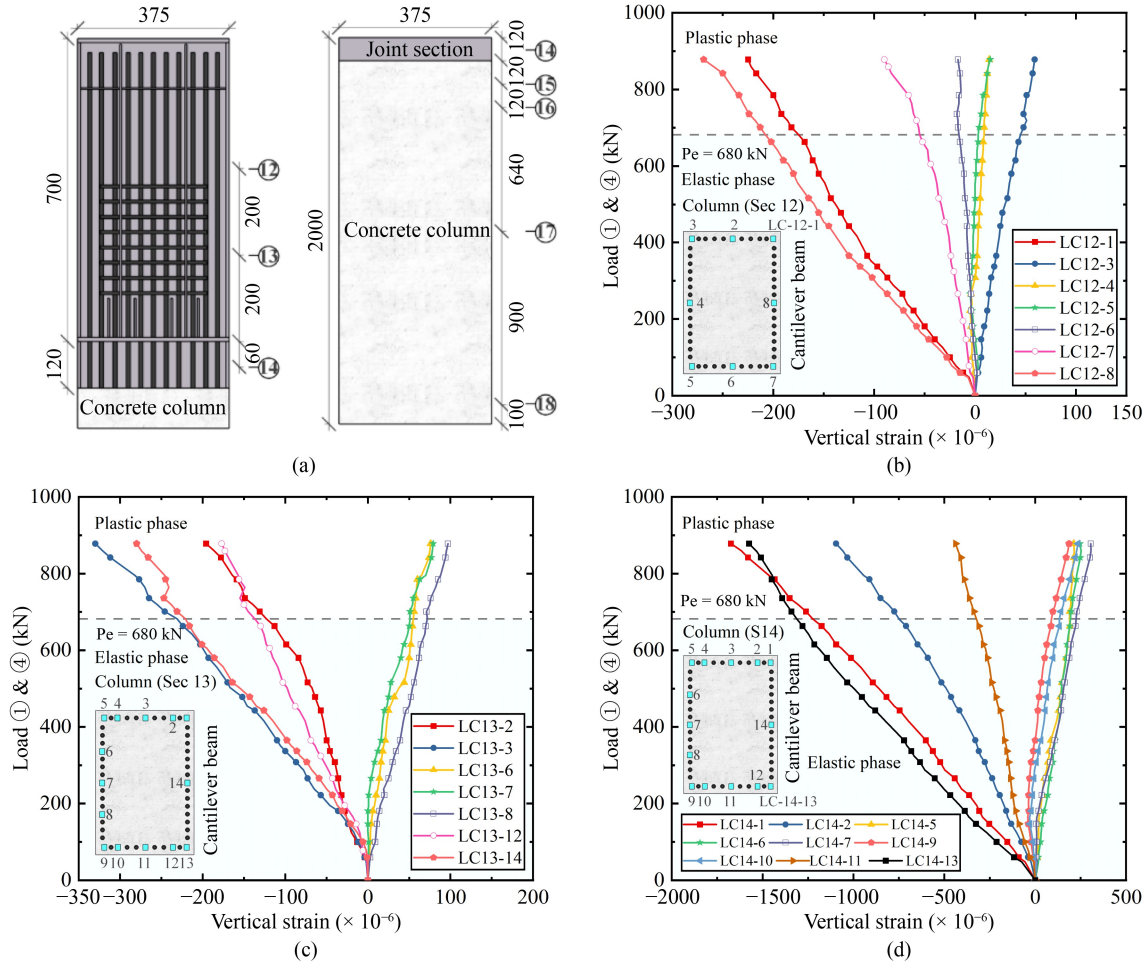

Fig. 15 Load–strain curve of the rebar-concrete connection: (a) test sections; (b) Section 12; (c) Section 13; (d) Section 14.

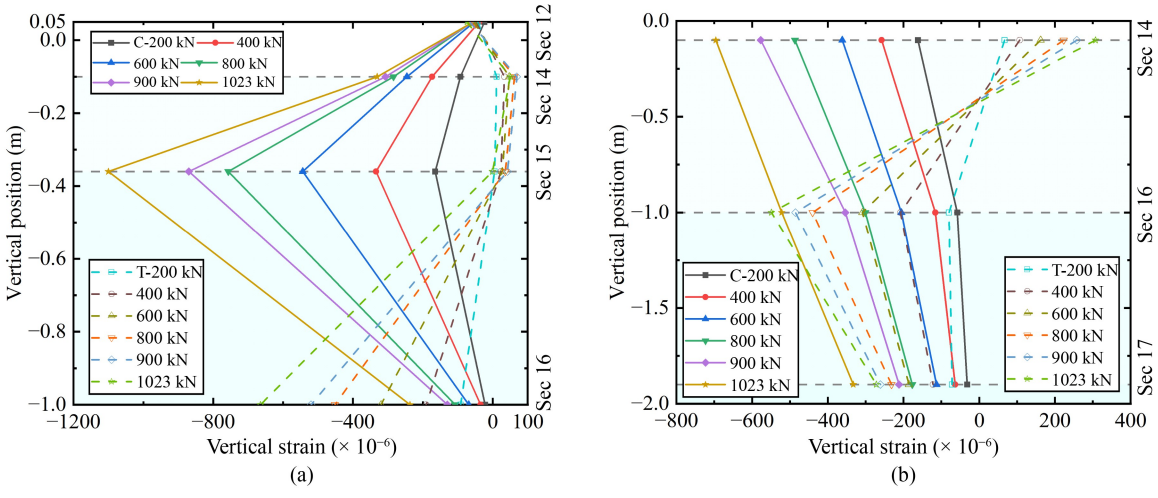

Fig. 16 The vertical strains along the column in specimen S2: (a) the rebars; (b) the concrete.

The following modeling approaches were employed. 1) The measured thicknesses of steel plates were used. 2) The bond between the rebars and concrete in the columns was assumed to be perfect with no slip, as the anchorage length was deemed sufficient. 3) The restraining effect of stirrups and other horizontal rebars was neglected. 4) Steel plates were modeled with nonlinear elastoplastic properties, while concrete and UHPC were treated as linear elastic materials due to its small elastic strain during the loading process and the absence of damage. Additionally, the nonlinear geometric effect was taken into account. 5) The initial geometric imperfection was

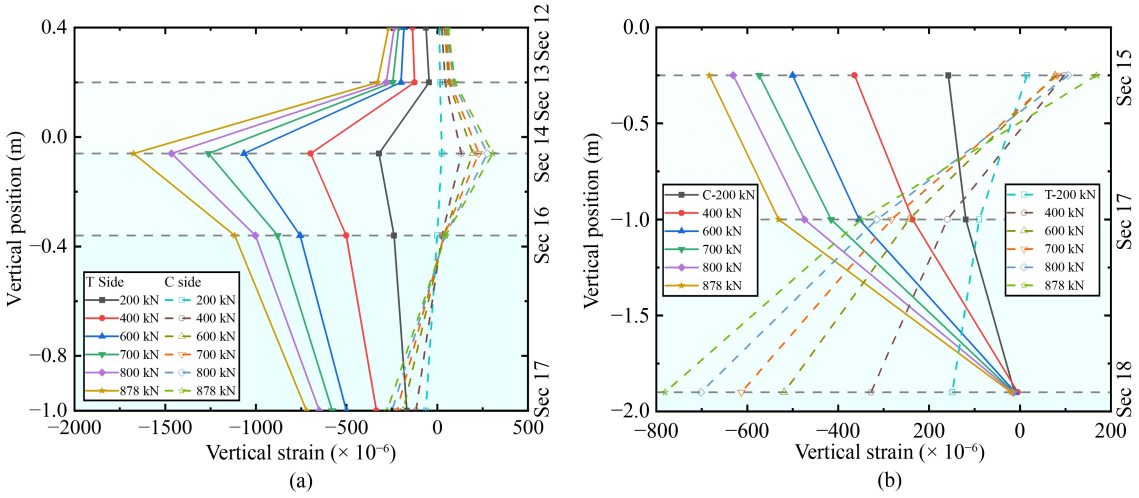

Fig. 17 The vertical strains along the column in specimen S2: (a) the rebars; (b) the concrete.

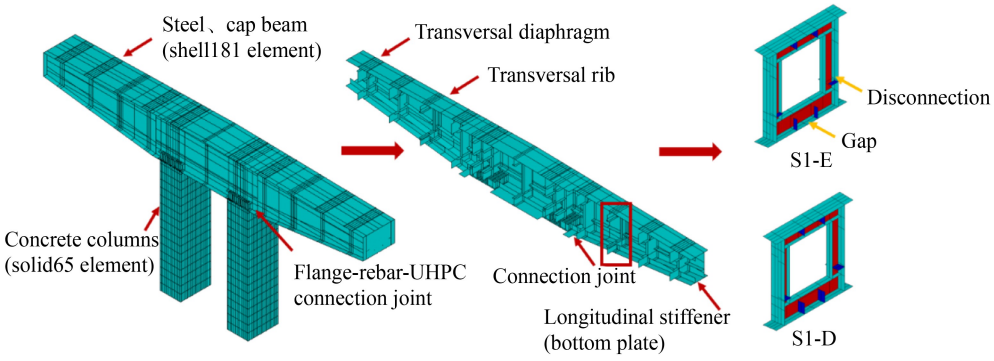

Fig. 18 FE models of specimen S1.

considered by adopting the global buckling mode under self-weight, with its maximum deformation set to $L/1000$ of the cantilever length. However, by comparing the 1st to 5th order buckling modes introduced as initial imperfections, the failure modes were consistent and the difference in ultimate bearing capacity was less than 1%, thus, the 1st order was applied.

As discussed in Subsection 5.1, structural detailing defects in the steel cap beams were identified as potential factors influencing overall structural performance. To quantitatively the influence, FE models were developed for both idealized piers without defects (designated as S1-D and S2-D) and piers incorporating representative defects (designated as S1-E and S2-E). In S1-E and S2-E, two defects were considered: the longitudinal stiffeners of the web and bottom plate were discontinued at all transverse diaphragms and ribs, and the transverse ribs were disconnected with the bottom plate with a 0.1 mm gap.

6.2 Finite element simulations compared with test results

The ultimate bearing capacities of FE models S1-E and S2-E were calculated following the same loading protocol in the experimental tests. Taking S2-E as an example, when the outer load was 870 kN, the vertical displacement of Section 1′ was 24.1 mm, which closely agreed with the test results of specimen S2 (the ultimate bearing capacity of 878 kN and maximum displacement of 21.5 mm), as shown in Fig. 19(a). Regarding the failure modes, both the simulation and experiment showed local buckling at the web plate between thickness-varying section and transverse rib as well as at the bottom plate below transverse rib, as shown in Fig. 19(b). Additionally, the load-strain curves of the top and bottom plates at Sections ①, ③, and ④ from the model were consistent with experimental data, as shown in Fig. 19(c). These results validated the accuracy of the FE models.

6.3 Influence of structural detailing defects on steel cap beam

The comparisons of the FE models S2-E (with defects), S2-D (without defects), S1-E, and S1-D are shown in Fig. 20. The failure mode of S2-E was the local buckling of web and bottom plates near the transverse ribs (Section 3′). In contrast, in S2-D, local buckling occurred at the web plate near the transverse diaphragm (Section 2′), and the maximum compressive stress occurred in the bottom

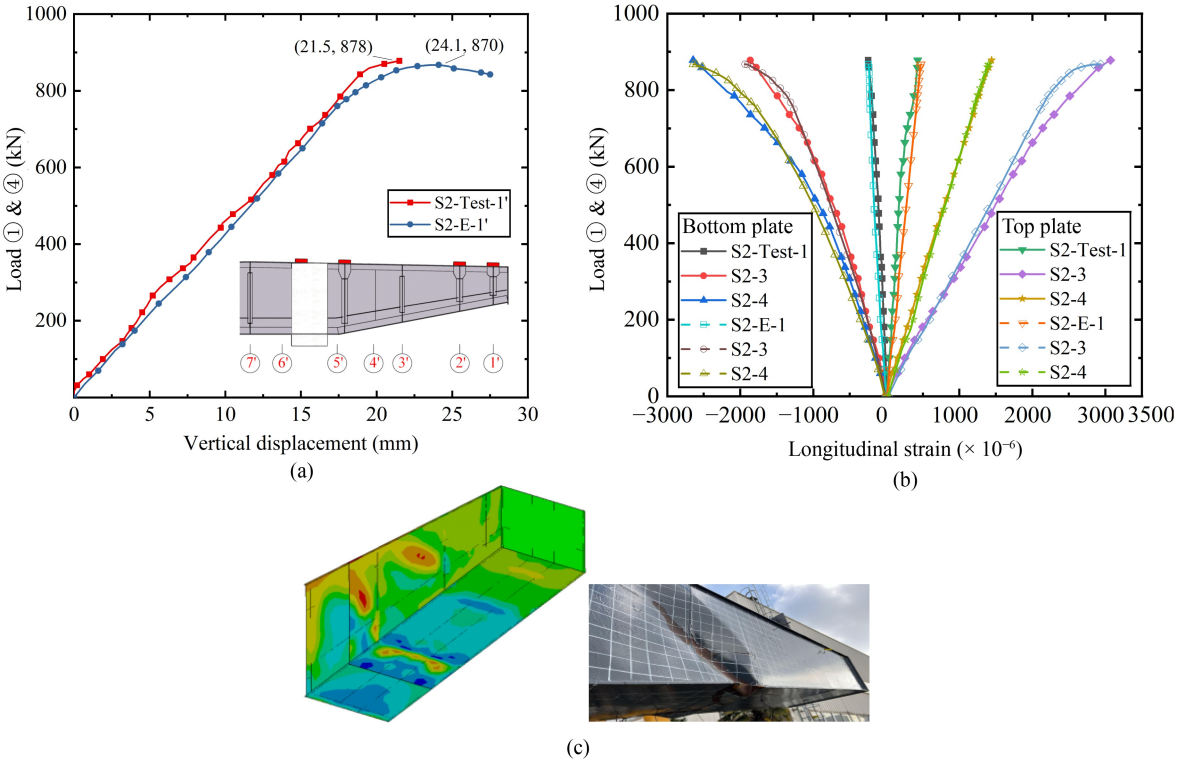

Fig. 19 The comparison between the test of specimen S2 and the FE model S2-E: (a) load–displacement curves; (b) load–strain curves; (c) failure modes.

plate at cantilever root (Section 5′). Similar changes in the failure modes and stress distributions due to the defects were also observed in the two FE models S1-D and S1-E.

By comparing the load-displacement curves of key sections between the FE models with and without structural detailing defects, S2-D exhibited higher ductility and load bearing capacity. Similarly, S1-D exhibited a higher stiffness and load bearing capacity.

Assuming the safety factor S as the ratio of the ultimate bearing capacity P_u to the load of serviceability limit state P_s, referring to the multiple by which the dead loads and live loads were scaled up simultaneously, as shown in Eq. (1). S of tests and FE models are summarized in Table 6.

$$S = P_u/P_s. \tag{1}$$

The FE analysis indicated the adverse effect on steel cap beam due to the defects of discontinuous longitudinal stiffeners and incomplete connection between the transverse diaphragm and bottom plate. These defects reduced local stiffness and induced the compressed bottom plates more susceptible to local buckling, thus leading to a declined ultimate bearing capacity. Overall, the safety factors of hybrid piers S1 and S2 without defects were estimated at 2.63 and 2.96, demonstrating adequate safety for practical engineering.

6.4 Influence of the construction sequence of the flange-rebar-ultra high performance concrete connection on concrete columns

As introduced in paragraph 3.1.3, traditional bridge construction typically involves completing the piers before erecting the main girders. The self-weight of main girders generates a large bending moment at the top of concrete columns, which can cause cracking issues. To address this issue, the π-shaped hybrid pier with the flange-rebar-UHPC connection and a unique construction sequence of hinged to rigid are proposed. The construction steps are as follows: 1) construct concrete columns; 2) install laminated rubber bearings on top of concrete columns; 3) place the steel cap beam and initially screw bolts; 4) install main girders onto the steel cap beam; 5) cast the UHPC and fully tighten the bolts. In this method, the steel cap beam and concrete column are not rigidly connected during the erection of main girders, and the laminated rubber bearing transmits only axial pressure with minimal bending moments from the steel cap beam to concrete columns. The cap beam-column joint becomes rigid only after the casting of UHPC and final tightening of bolts. Therefore, the top of concrete column is only subjected to bending moments generated by vehicle loads and dead loads of ancillary components on main girders, which improves the stress condition.

The FE model S1-D was used to analyze the influence

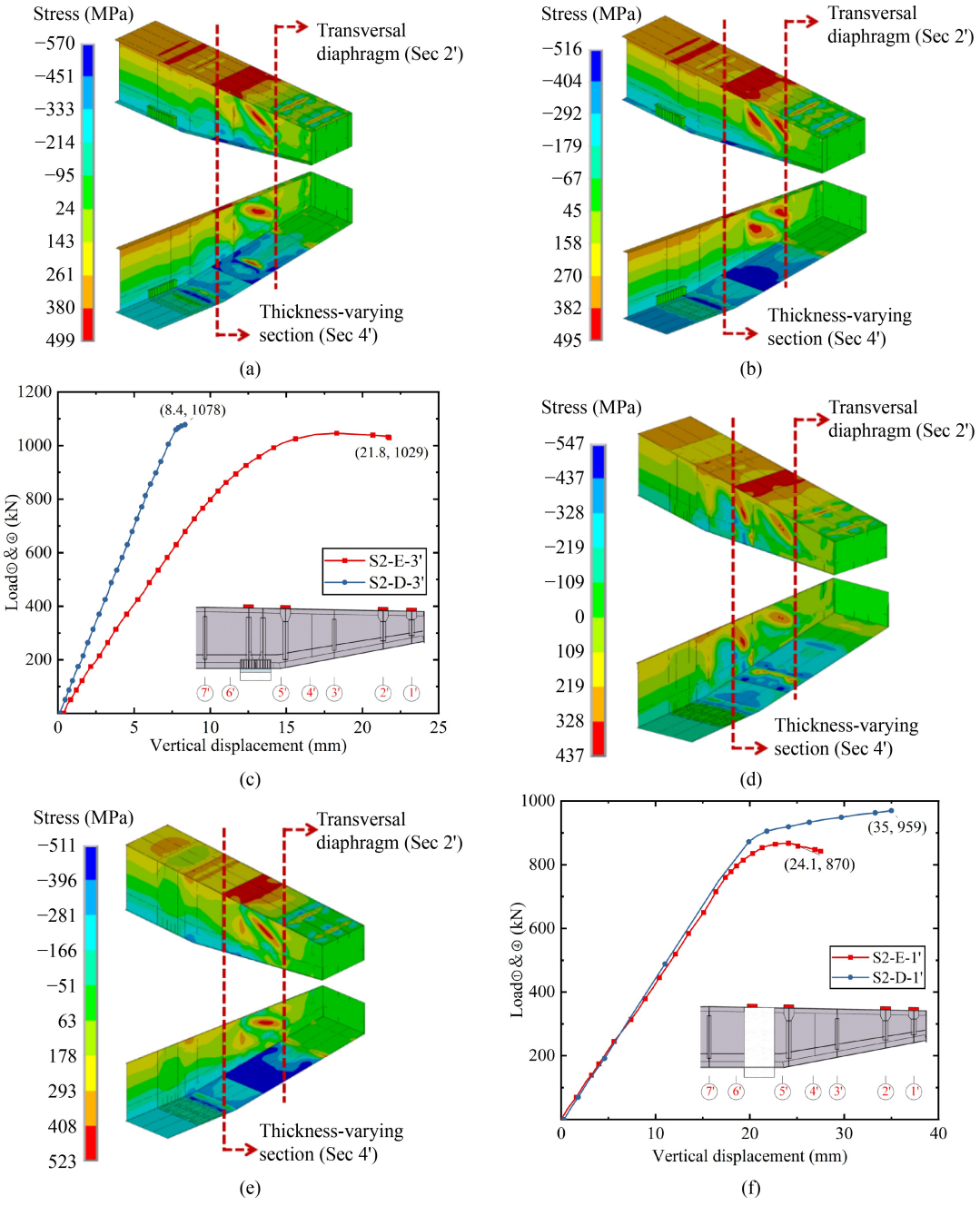

Fig. 20 The comparison of the FE simulations with/without structural detailing defects: (a) longitudinal stress of S1-E; (b) longitudinal stress of S1-D; (c) load–displacement curve of S1; (d) longitudinal stress of S2-E; (e) longitudinal stress of S2-D; (f) load–displacement curve of S2.

of the construction sequence of the flange-rebar-UHPC connection on structural behavior of concrete columns. The load of serviceability limit state (*PL*) is considered. Fig. 21 shows the results. 1) The cantilever root of steel cap beam exhibited the highest compressive stresses in both construction methods, while the compressive stress was 16% lower when using the innovative method than using the traditional method. 2) The Side C at the top of concrete column was under vertical compression and Side T was under tension. The new connection and construction method reduced vertical compressive and tensile stress by 20% and 49%, respectively. Notably, the significant reduction in vertical tensile stress is particularly important for mitigating concrete cracking.

7 The actual project

Comprehensively considering the factors of structural performances, construction efficiency, economy, social

and environmental impacts, the π-shaped hybrid piers with the flange-rebar-UHPC connection were finally selected for the practical project. Figure 22 illustrates the construction procedure. The concrete columns were assembled on site using precast segments. The steel cap beams were manufactured as a unit in factory and subsequently transported to the construction site for assembly.

8 Conclusions

This study proposes a novel π-shaped hybrid pier with prefabricated large-cantilevered steel cap beams and concrete columns, as well as two innovative joints, i.e., the flange-rebar-UHPC connection and the rebar-concrete connection. Two large-scale (1:4) specimens of the π-shaped hybrid piers with the two different joints were tested. Based on the tests, the FE method was used to further study the structural behavior of the π-shaped hybrid piers. The following conclusions can be drawn.

1) The cantilever structure of steel cap beams was subject to bending moments and shear forces, and the plate thickness-varying design fully utilized the strength of steel plates. Steel yielding initiated at the bottom plate at the cantilever root section in specimen S1, and at the top plate at the thickness-varying section in specimen S2, respectively.

2) The ultimate bearing capacity of specimens S1 and S2 was 1023 and 878 kN, respectively. Local buckling occurred in the web and bottom plates of the steel cap beams. The maximum downward displacements at the cantilever ends of specimen S1 and S2 were 59.8 and 21.5 mm, respectively, indicating good structural ductility. Furthermore, the cap beam–column joints and concrete columns of the two specimens in the state of small eccentric compression were basically in the elastic phase when the steel cap beams failed.

3) FE analysis indicated that the structural behavior of the steel cap beams was affected by structural details. Discontinuity of longitudinal stiffeners and incomplete connection between the transverse diaphragm and bottom plate reduced local stiffness and plate buckling resistance, leading to decreased ultimate bearing capacity. In addition, the safety factors of S1 and S2 were 2.41 and 2.82 in tests, and those of S1 and S2 without defects were estimated at 2.63 and 2.95 in FE analysis, fulfilling the safety demand for practical engineering.

4) By using the proposed construction sequence for the π-shaped hybrid piers with the flange-rebar-UHPC connection, the top of concrete column was only

Table 6 The safety factors

Item	P_u (kN)	PL (kN)	S
S1	1023	364	2.81
S1-E	1029	–	2.83
S1-D	1078	–	2.96
Improvement of S1-D to S1-E	–	–	4.6%
S2	878	364	2.41
S2-E	870	–	2.39
S2-D	959	–	2.63
Improvement of S2-D to S2-E	–	–	10.0%

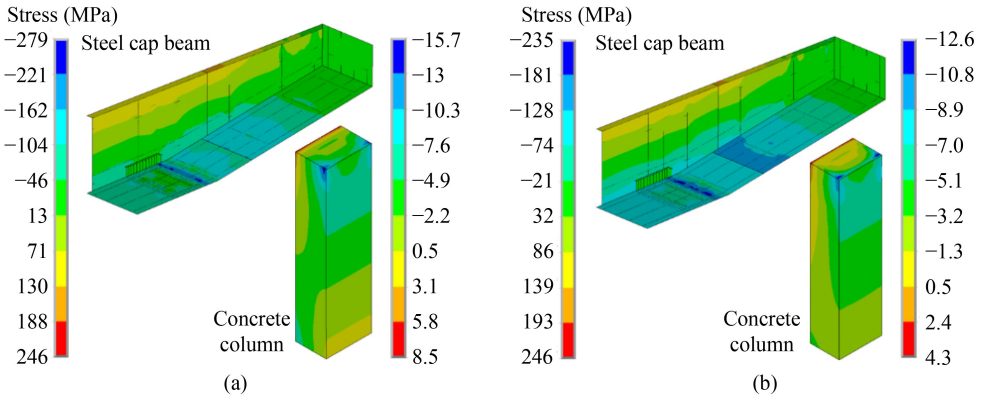

Fig. 21 The comparison of traditional and innovative construction methods: (a) traditional construction method; (b) innovative construction method.

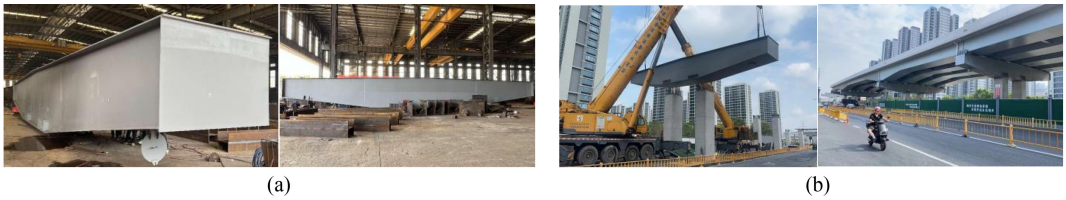

Fig. 22 The construction of the actual bridge project: (a) the steel cap beam; (b) the construction on site.

subjected to the bending moment generated by vehicle loads and dead loads of ancillary components on main girders (the bending moments due to the self-weight of main girders were released). Therefore, the vertical compressive and tensile stress were reduced by 20% and 49%, respectively. Such reduction in tensile stress significantly mitigated the potential cracking problem of concrete columns.

5) Through comprehensive comparisons, the π-shaped hybrid piers with large-cantilevered steel cap beams and concrete columns exhibited advantages in terms of self-weight, transportation, aesthetic appearance, construction timeline, and carbon emissions, despite their slightly higher costs compared to traditional concrete piers. These hybrid piers align well with the strategic objectives for rapid construction, high-quality prefabrication, and green buildings, and they are particularly suitable for urban viaducts with wide roadways. The hybrid piers with the flange-rebar-UHPC connection have been successfully applied in the actual bridge, which has been operating safely to date.

Acknowledgement Supports from the National Natural Science Foundation of China (Grant No. 52478197) are acknowledged. Supports for Chong Shen from the China Scholarship Council (No. 202306260161) are acknowledged. The authors also acknowledge the supports and assistance from Tongji Architectural Design (Group) Co., Ltd. and Shanghai TXMEC Technology Co., Ltd.

Competing interests The authors declare that they have no competing interests.

References

1. Reddemann T. “Express bridge” rapid construction system-systematic-development of rapid bridge construction systems as an answer to the renovation backlog of the traffic infrastructure and the associated problems. Beton-und Stahlbetonbau, 2021, 116(52): 48–59
2. Wang X, Li W S, Liu Z. Experimental investigation and fragility analysis on seismic performance of precast UHPC hollow piers under varying axial load. Soil Dynamics and Earthquake Engineering, 2025, 196: 109420
3. Shao X D, Zeng H Q, Cao J H. Flexural behavior of fully prefabricated large-cantilevered high strength steel-UHPC composite bent caps. Journal of Constructional Steel Research, 2023, 204: 107856
4. Matsumoto E E, Waggoner M C, Kreger M E, Vogel J, Wolf L. Development of a precast concrete bent-cap system. PCI Journal, 2008, 53(3): 74–99
5. Hu H, Wang J W, Yan X F, Ge J, Zhang D. Experimental research and numerical analysis on mechanical behavior of lightweight-design precast bent caps with large cantilevers. Structures, 2022, 40: 536–554
6. Culmo M P. Connection Details for Prefabricated Bridge Elements and Systems. Federal Highway Administration, Office of Bridge Technology, 2009
7. Lee H, Cho D, An Z, Chung W. Composite behavior of steel I-girders connected to inverted-T bent cap. International Journal of Steel Structures, 2015, 14(4): 711–721
8. Li Z Q, Leiva J D. Pretensioned, precast concrete hollow-core units used for interchanged bridge project in Honduras. PCI Journal, 2010, 55(1): 71–78
9. Hu F J, Yang C H, Zhou P M, Hu H, Wang Y. Experimental study on mechanical behavior of precast large-cantilevered UHPC bent caps with π-shaped cross-sections. Structures, 2024, 62: 106333
10. McKee C D, Lee J D, Birely A C, Mander J B. Experimental behavior of pretensioned bent caps with internal voids for weight reduction. Journal of Bridge Engineering, 2020, 25(1): 04019123
11. Xu D, Xiang H F, Huang D Y. Model test of segmental concrete coping with unbonded prestressing stands. Structural Engineer, 1999, 15(1): 29–32
12. Ge J P, Mei D L, Yan X F. Comparison and analysis of construction method of precast pier cap. Journal of Technology, 18(1): 56–62
13. Birely A C, Yole K J, Lee J D, Mckee C D, Mander J B. Experimental behavior of reinforced concrete and pretensioned concrete bent caps. Journal of Bridge Engineering, 2020, 25(2): 04019137
14. Saibabu S, Srinivas V, Sasmal S, Lakshmanan N, Iyer N R. Performance evaluation of dry and epoxy jointed segmental prestressed box girders under monotonic and cyclic loading. Construction and Building Materials, 2013, 38: 931–940
15. Xia Z H, Zhang Z J, Li Y L, Xia J. Experimental investigation and prediction of load carrying capacity of a novel UHPC-shell strengthened prefabricated concrete bent cap. Case Studies in Construction Materials, 2022, 17: e01684
16. Ye M, Li L F, Hu F J, Wang L, Shao X. UHPC-based precast large-cantilevered thin-walled bent caps: Design and experiments. Engineering Structures, 2022, 272: 114909
17. Li L F, Ye M, Hu F J. Experimental study on the flexural behavior of a prefabricated large-cantilevered prestressed UHPC thin-walled bent cap. China Civil Engineering Journal, 2020, 53(02): 92–104 (in Chinese)
18. Li J W, Xia Z H, Sun M S, Xia J. Experimental study on mechanical performance of UHPC formwork-RC composite cap beam. China Journal of Highway and Transport, 2021, 34(8): 157–167
19. Ma X M. Construction technology of fabrication and hoisting of steel cover girder spanning over Beijing-Shanghai high-speed railway. Railway Engineering, 2013, 53(8): 38–40
20. Zhou W J. Analysis on application of steel capping beam in municipal elevated bridge. Urban Roads Bridges & Flood Control, 2021, 38(6): 313–317
21. Meng L Q, Li Y S, Wang Y Q. Finite element analysis of bearing performance of viaduct steel cap. Journal of Shijiazhuang Railway University, 2009, 22(1): 38–42
22. Kitada T. Ultimate strength and ductility of state-of-the-art concrete-filled steel bridge piers in Japan. Engineering Structures, 1998, 20(4–6): 347–354
23. Kitada T, Matsumura M, Otoguro Y. Seismic retrofitting

techniques using an energy absorption segment for steel bridge piers. Engineering Structures, 2003, 25(5): 621–635
24. Yamada T, Numata K, Haru B. Two-girder rigid frame bridge combining girders and RC pier. Research and Development Kobe, 2003, 53(1): 19–26
25. Nakamura S, Momiyama Y, Hosaka T, Homma K. New technologies of steel/concrete composite bridges. Journal of Constructional Steel Research, 2002, 58(1): 98–130
26. Matusi S, Yukawa Y, Wada N. A study on the design for rigid connection of steel girder and RC pier in hybrid frame bridge. Journal of Structural and Construction Engineering, 1997, 43(495): 1367–1374
27. Suzuki Y, Mizuguchi K, Yoshida M. A rigid connection mechanism of composite frame bridge ad its model loading test. Journal of Structural and Construction Engineering, 1998, 44: 1435–1446
28. Iwasaki H, Nishido T. Mechanical characteristics of rigidly connected girders and concrete piers with perfobond rib shear connectors. Steel Construction Engineering, 2003, 10(38): 119–128
29. Ji B H, Gao J M, Aoki T. Static cyclic-loading test on new type of rigid connection of steel girder and reinforced concrete pier. Journal of Southeast University, 2003, 19(4): 368–372
30. Liang Q Z, Guo W H. Optimal design of connection details of steep cap beam and concrete pier column based on integral joint concept. Bridge Construction, 2024, 54(3): 129–134
31. Xie W, Zhang B, Yu L. Flexural performance of an innovative girder-to-pier joint for composite bridges with integral piers: Full-scale test. Materials, 2025, 18(5): 1157
32. Wang S Z, Su Q T, Jiang X, Michels J, Ghafoori E. Fully bonded iron-based shape memory alloy for retrofitting large-scale bridge girders: Thermal and mechanical behavior. Structures, 2024, 65: 106710
33. Liu B F, Su Q T, Wang S Z, Wang F. Experimental and numerical study of riveted joints in truss bridges reinforced with added steel plates. Thin-Walled Structures, 2025, 214: 113314
34. Jiang C, Wu C, Jiang X. Experimental study on fatigue performance of corroded high-strength steel wires used in bridges. Construction and Building Materials, 2018, 187: 681–690
35. Shanghai Construction Market Information Service Platform. 2020
36. GB/T 51366-2019 Standard for Calculation of Building Carbon Emissions. Beijing: China Architecture and Building Press, 2019
37. JTG D60-2015. General Specifications for Design of Highway Bridge and Culvert. Beijing: Ministry of Transport of the People's Republic of China, 2015
38. GB/T 228.1-2021. Metallic Materials-Tensile Testing-Part 1: Method of Test at Room Temperature. Beijing: Standardization Administration of the People's Republic of China, 2021
39. GB 50017-2017 Code for Design of Steel Structures. Beijing: China Architecture and Building Press, 2017
40. GB/T 50081-2019 Standard for Test Methods of Physical and Mechanical Properties of Concrete. Beijing: China Architecture & Building Press, 2019